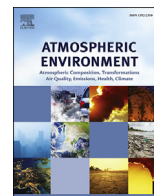




Contents lists available at ScienceDirect

Atmospheric Environment

journal homepage: www.elsevier.com/locate/atmosenv

Anthropogenic sulphur dioxide load over China as observed from different satellite sensors



M.E. Koukouli^{a,*}, D.S. Balis^a, Ronald Johannes van der A^b, N. Theys^c, P. Hedelt^d,
A. Richter^e, N. Krotkov^f, C. Li^{f,g}, M. Taylor^a

^a Laboratory of Atmospheric Physics, Aristotle University of Thessaloniki, Thessaloniki, Greece

^b Royal Netherlands Meteorological Institute (KNMI), De Bilt, The Netherlands

^c Belgian Institute for Space Aeronomy, Brussels, Belgium

^d German Aerospace Center, Remote Sensing Technology Institute, Germany

^e Institute of Environmental Physics, University of Bremen, Bremen, Germany

^f NASA Goddard Space Flight Center, Greenbelt, MD, USA

^g Earth System Science Interdisciplinary Center, College Park, MD, USA

HIGHLIGHTS

- SCIAMACHY/Envisat, OMI/Aura and GOME2/MetopA SO₂ columns over China are presented.
- Monthly mean time series of megacities and known power plant locations are examined.
- 90% of the locations studied show a sharp decline in SO₂ emissions this past decade.
- 70% of the locations have a statistically significant annual cycle with highs in winter.
- The implementation of government desulphurisation legislation over China is effective.

ARTICLE INFO

Article history:

Received 30 June 2016

Received in revised form

1 September 2016

Accepted 3 September 2016

Available online 6 September 2016

Keywords:

Sulphur dioxide

China

Satellite remote sensing

OMI

SCIAMACHY

GOME2A

Trends

Seasonality

ABSTRACT

China, with its rapid economic growth and immense exporting power, has been the focus of many studies during this previous decade quantifying its increasing emissions contribution to the Earth's atmosphere. With a population slowly shifting towards enlarged power and purchasing needs, the ceaseless inauguration of new power plants, smelters, refineries and industrial parks leads infallibly to increases in sulphur dioxide, SO₂, emissions. The recent capability of next generation algorithms as well as new space-borne instruments to detect anthropogenic SO₂ loads has enabled a fast advancement in this field. In the following work, algorithms providing total SO₂ columns over China based on SCIAMACHY/Envisat, OMI/Aura and GOME2/MetopA observations are presented. The need for post-processing and gridding of the SO₂ fields is further revealed in this work, following the path of previous publications. Further, it is demonstrated that the usage of appropriate statistical tools permits studying parts of the datasets typically excluded, such as the winter months loads. Focusing on actual point sources, such as megacities and known power plant locations, instead of entire provinces, monthly mean time series have been examined in detail. The sharp decline in SO₂ emissions in more than 90%–95% of the locations studied confirms the recent implementation of government desulphurisation legislation; however, locations with increases, even for the previous five years, are also identified. These belong to provinces with emerging economies which are in haste to install power plants and are possibly viewed leniently by the authorities, in favour of growth. The SO₂ load seasonality has also been examined in detail with a novel mathematical tool, with 70% of the point sources having a statistically significant annual cycle with highs in winter and lows in summer, following the heating requirements of the Chinese population.

© 2016 Elsevier Ltd. All rights reserved.

* Corresponding author.

E-mail address: mariliza@auth.gr (M.E. Koukouli).

1. Introduction

Sulphur dioxide emissions in China have long interested the scientific community, both from the modelling aspects as well as the study of the remote sensing observations of SO₂. In the work of Lu et al., 2010, it was shown that from 2000 to 2006, the total SO₂ emissions in China increased by 53%, with power plants contributing around half of that increase. Furthermore, a clear North-South gradient was revealed, with Northern provinces increasing their emissions by 85%, whereas the Southern values increased by only 28%. In the same work, it was shown that the growth rate in SO₂ emissions slowed around year 2005 and exhibited a decrease after 2006, mainly due to the widespread application of flue-gas desulfurization devices (FGD) in power plants in response to a new policy of the Chinese government (Lu et al., 2010; Klimont et al., 2013), also reported that, while China is the largest single contributor of SO₂ emissions (supplying around 30% of total global emissions), Chinese SO₂ emissions peaked around 2006 followed by a decline towards 2011. Satellite observations have since verified these findings, as discussed in the work of Li et al., 2010, showing substantial increases in SO₂ and tropospheric column NO₂ OMI/Aura observations from 2005 to 2007 over several areas in northern China where large coal-fired power plants were built during this period (Zhang et al., 2009), as well as dramatic reductions in SO₂ for 2008. These reductions further confirm the effectiveness of FGD devices, as also extensively discussed by Lu et al., 2010. The recent work of Krotkov et al., 2016, has extended the time period examined to 2014, confirming the continued decrease in SO₂ emissions from 2010 onwards in the context of a further reduction associated with the ongoing global economic crisis.

The inherent potential of different satellite instruments to sense strong SO₂ sources has been long demonstrated in literature; from the era of Nimbus 7/TOMS and GOME/ERS-2 where volcanic eruptions and outgassing (Krueger, 1983; Eisinger and Burrows, 1998) as well as lignite burning from Eastern European power plants (Zerefos et al., 2000) were identified, all the way to OMI/Aura monitoring of the air quality over Canadian oil sands (McLinden et al., 2012, 2014). Anthropogenic sources such as copper smelters, fires in sulphur plants, coal-fired power plants, heavy metal smelting and so on, have been identified in numerous works and a variety of satellite sensors, see for e.g. the works of Carn et al., 2004, 2007; De Foy et al., 2009; Fioletov et al., 2013; Bauduin et al., 2014, among others. Similarly, volcanic outgassing and eruptive events have been revealed for e.g. by Khokhar et al., 2005, Lu et al., 2013, Carn et al., 2015, among others. In this work, the SO₂ atmospheric load over China as reported by SCIAMACHY/Envisat, OMI/Aura and GOME2/MetopA is presented. The funding behind this line of investigation originates in the FP7 European Union Marco Polo/Panda project which aims to study air quality over China using a variety of space-born observational tools and modelling techniques [<http://www.marcopolo-panda.eu/>]. Scientists, local authorities, municipal and provincial level decision-makers are to benefit from the latest that air quality monitoring technology has to offer. The only disadvantage of current satellite instrumentation in air quality science is the fact that the aforementioned sensors all fly on polar orbiting platforms, hence providing, at best, two measurements per location per day. This fact makes it impossible to study the daily variability of the tropospheric pollutants of interest to air quality, an important piece of information for the short lived species, such as the NO_x family of gases. However, a number of geostationary orbiting satellites carrying air quality monitoring instruments are due to become operational during the next decade; Korea with GEMS (*Geostationary Environment Monitoring Spectrometer*; Lasnik et al., 2014) to be flown on GeoKOMPSAT-2B, Europe (ESA and EUMETSAT) with

the UVNS (*UV NIR Spectrometer*; http://esamultimedia.esa.int/docs/EarthObservation/Sentinel4_facts_2015.pdf) on Sentinel-4 and NASA with TEMPO (*Tropospheric Emissions: Monitoring of Pollution*; Zogman et al., 2016) will cover Asia, Europe and America respectively with hourly measurements on a fine spatial resolution. Those instruments will bring innumerable new possibilities in the field of emission monitoring from space. The work reported here does not aim to inter-compare, evaluate or perform inter-satellite validation of the SO₂ estimates obtained by different sensors and algorithms. The paper wishes to present the vertical column density (VCD) data reported by each algorithm and assess their individual strengths and shortcomings in particular for studying the SO₂ atmospheric load over China. The main premise is that almost all these are official datasets that an independent user should be able to simply download and post-process for her/his scientific needs, and this paper will proceed with this line of enquiry in mind. To be more specific, the main goals of this paper are the following:

- i. Firstly to demonstrate the potential of the SCIAMACHY/Envisat, OMI/Aura and GOME2/MetopA satellite instruments and algorithms to observe the anthropogenic SO₂ load over China. The focus is on presenting the optimum spatial and temporal scales needed in order to achieve an adequate signal-to-noise ratio for each sensor.
- ii. Secondly, to identify SO₂ emitting point sources separately for each instrument and algorithm. Here, attention is given to pixel size and the effect of data gridding onto regular maps. The effect of local point sources on surrounding regions is also discussed.
- iii. Thirdly, to demonstrate that significant trends per point source can be observed when the appropriate post-processing has been performed. Furthermore, special cases of locations with positive trends, possible dust incursion effects and/or strong seasonal signals, are identified and discussed.

The datasets are presented in Section 2 with the GOME2/MetopA GDP4.7 SO₂ product, the SCIAMACHY/Envisat SGP5.02 product, the OMI/Aura NASA PCA product and the OMI/Aura BIRA algorithm product discussed in Sections 2.1, 2.2, 2.3 and 2.4 respectively. In the various sub-sections of Section 3, we describe the analysis and associated findings. Finally, the main findings and conclusions are summarized in Section 5.

2. The datasets

In this work, sulphur dioxide columns reported as Vertical Column Densities, VCDs, by the SCIAMACHY/Envisat, OMI/Aura and GOME2/MetopA instruments are studied. Traditionally, in comparison and evaluation works such as the one by Fioletov et al. (2013), the Slant Column Density [SCD] is examined so that the application of a common air mass factor [AMF] will lead to comparable results. However, as stated in the introduction, in this work we aim to demonstrate the benefits that each reported VCD provides without delving into the intricacies of each algorithm.

The domain considered extends from 60° to 135°E and from 20° to 55°N and covers all of China as well as parts of the Far East. The data were filtered for high Solar Zenith Angle, SZA, of >70°, cloud fraction, of >0.2 and also SO₂ algorithm flagging. The filtered data were then averaged onto a 0.25° × 0.25° monthly grid using a 0.75° smoothing average box.

The provenance of each dataset is discussed in the following four sub-sections.

2.1. GOME2/MetopA GDP 4.7 algorithm

GOME-2 on board the MetopA satellite measures UV Earthshine spectra with a ground pixel size of $80 \times 40 \text{ km}^2$ on a 1920 km broad swath, thus allowing for a near global coverage within 1.5 days (Munro et al., 2016). Once per day a solar irradiance spectrum is recorded that is used for the calculation of an Earth reflectance spectrum. A comprehensive review of the instrument and the current status of its products may be viewed in Hassinen et al., 2016. SO_2 vertical columns are retrieved on an operational basis with the GDP 4.7 algorithm in the framework of EUMETSAT's Satellite Application Facility for Atmospheric Composition and UV Radiation, O3M-SAF, project. First, a DOAS retrieval is performed in the wavelength region 315–326 nm, in which cross-sections of SO_2 (Bogumil et al., 2003), O_3 (Brion et al., 1993) and NO_2 (Gür et al., 2005) are fitted to the UV Earth reflectance spectrum (see Rix et al., 2012 for further details). The retrieved SO_2 slant column is then corrected for any instrumental bias by applying a latitude and surface-altitude dependent offset correction. The correction factors are determined in a 14-days moving time window. The resulting slant columns are then corrected for the atmospheric temperature in which SO_2 is expected. Secondly, the background and temperature corrected slant columns are converted to total vertical columns (VCDs) by means of an Air Mass Factor (AMF), which takes into account the viewing geometry, surface and cloud parameters as well as an a priori SO_2 profile shape. Since at the time of the measurement it is unknown at which altitude the SO_2 layer is located, the user is provided with a set of three SO_2 results for pre-defined SO_2 profile scenarios. For each of these scenarios a single-wavelength AMF at 320 nm is applied. It is based on an SO_2 profile with the centre of mass at prescribed altitudes. For this paper the VCD calculated with an SO_2 centre of mass located at 2.5 km was chosen. The GOME-2A GDP4.7 have been formally validated as part of the official EUMETSAT O3MSaf project (Theys et al., 2013). We should note here, as a preamble to what follows, that there exists an unavoidable instrumental effect in orbit; instruments measuring in the UV/Vis regions are known to be sensitive to effects of contamination and to degradation of their optical elements. The impact of GOME-2 instrument degradation on Level-2 product quality is very much dependent on the spectral region and the type of retrieval methods chosen (EUMETSAT, 2012) and has been quantified in Dikty et al. (2011).

In the following, the forward scan observations of the descending node of the GOME-2 flight path were used over the time period between January 2007 to December 2014. The data have been downloaded from <http://atmos.eoc.dlr.de/gome2/>.

2.2. SCIAMACHY/Envisat SGP 5.02 algorithm

The Scanning Imaging Absorption spectroMeter for Atmospheric Cartography (SCIAMACHY) was launched in March 2002 aboard the European platform ENVISAT and has been operational for more than ten years providing global coverage in approximately six days (Bovensmann et al., 1999) up until April 2012. ENVISAT was in a sun-synchronous orbit with an inclination of 98.5° , a mean altitude of 796 km and had a period of 100 min, performing 14 or 15 orbits per day with an Equator crossing time of 10:00 local time. The nominal swath was 960 km with a typical footprint size of $60 \text{ km} \times 30 \text{ km}$ for SO_2 observations. The current version of the operational algorithm SGP version 5.02, as well as the format of the level-2 total SO_2 columns are described in detail in the relevant Products Quality Readme File (SCIAMACHY Readme File, 2011) and the Algorithm Theoretical Baseline Description, ATBD, (SCIAMACHY ATBD, 2015). In short, the fitting interval is between 315 and 327 nm, while a 3rd order polynomial is being fitted. The

absorption cross sections come from Vandaele et al. (1994), the background reference sector is from the Pacific region, around 180° – 220° , while an inverse spectrum of Earthshine radiance is used for offset and slope correction. The AMF reference wavelength is at 315 nm and for the anthropogenic case used here a pollution scenario of 1 DU SO_2 for the first kilometre from the ground is assumed. It is strongly recommended that the SCIAMACHY DGP5.02 Boundary Layer SO_2 product should only be used for the largest signals and should be cross-checked against other data sets, which is the sideways result of this work. As suggested in the Readme File, only the forward scan observations are accepted over the time period between January 2004 and December 2011. The data have been downloaded from <https://earth.esa.int/>

2.3. OMI/Aura NASA algorithm

The NASA standard OMI/Aura Planetary Boundary Layer, PBL, SO_2 VCD data are produced with an innovative Principal Component Analysis (PCA) algorithm (Li et al., 2013). This algorithm employs a PCA technique to extract a set of principal components (PCs) from satellite-measured radiances in the spectral range of 310.5–340 nm. The leading PCs that explain the most spectral variance are generally associated with both physical processes (e.g., O_3 absorption and rotational Raman scattering) and measurement artefacts (e.g., wavelength shift) that may interfere with SO_2 retrievals. When the PCs are used in the spectral fitting, they can help account for these various interfering factors in SO_2 retrievals, leading to reduced retrieval noise and biases. The current operational OMI PBL SO_2 product uses a simplified Jacobian lookup table calculated assuming fixed solar and viewing zenith angles ($\text{SZA} = 30^\circ$, $\text{VZA} = 0^\circ$), cloud-free conditions, surface albedo = 0.05 and O_3 VCD = 325 D.U. for all pixels. The algorithm also assumes that SO_2 load is predominantly in the lowest 1000 m of the atmosphere. This may lead to biases particularly under partially cloudy conditions and a new generation algorithm with a more comprehensive lookup table is currently being developed. Details about the PCA algorithm can be found in Li et al., (2013). The data used in this work have been downloaded from <https://disc.sci.gsfc.nasa.gov/> for the time period examined between January 2005 and December 2014. Following current updates on the OMI row index anomaly [<http://omi.fmi.fi/anomaly.html> and KNMI, 2012] only pixels in rows between 5 and 23 were accepted.

2.4. OMI/Aura BIRA algorithm

The retrieval of SO_2 VCDs using the BIRA algorithm is achieved by applying Differential Optical Absorption Spectroscopy (DOAS) (Platt and Stutz, 2008) to the measured spectra in the 312–326 nm wavelength range. This is followed by a data filtering for the row-anomaly and a background correction to account for possible biases on the retrieved slant columns. The obtained quantity is converted into an SO_2 VCD using an air mass factor that accounts for changes in measurement sensitivity due to observation geometry, ozone column, clouds, and surface reflectivity. The air mass factor calculation is made for anthropogenic SO_2 profile shapes from the IMAGES tropospheric chemistry transport model. More details on the BIRA OMI SO_2 algorithm can be found in Theys et al. (2015). This dataset, provided for the period January 2005 to December 2014, have been flagged accordingly.

3. Data screening and optimal gridding choices for an SO_2 anthropogenic signal over China

Section 3.1 aims to cover the first of the two aims of this paper, namely the discussion of the different gridding, mapping, filtering,

etc, techniques that may be applied to satellite SO₂ observations before those can provide a statistically significant result. Contrary to what has been shown in previous works [for e.g. in Fioletov et al., 2011; Lee et al., 2011] the winter months are not excluded in this analysis as they form an important part of the SO₂ seasonal cycle. In the beginning of the Section, different masking choices on monthly SO₂ gridded maps over China are considered and the resultant yearly averages are presented. Locations of SO₂ emitting sources around the domain is also discussed. In Section 3.2, the monthly mean time series around the SO₂ locations are discussed, including the screening process and the calculation of statistically significant trends, hence covering the third aim of this paper. Special cases of interest, such as locations with a positive trend and locations affected by possible dust events with signatures in the SO₂ observations [Section 4.1], as well as the study of seasonality in the SO₂ loading over China [Section 4.2] using novel mathematical tools, based on the OMI/Aura BIRA dataset, complete this study.

3.1. SO₂ loading over Eastern China

Even though some minor differences between the instructions given by the PIs of the different algorithms exist, they all converge that a restriction should be applied in the manipulation of the SO₂

columns on both the cloud fraction and the solar zenith angle associated with the measurement (Fioletov et al., 2011; Theys et al., 2015). For the cloud fraction, a value between 0.2 [i.e. 20% cloud coverage in the satellite pixel] and 0.3 [30%] is the best cut-off level for the anthropogenic [or PBL] SO₂ columns as the optimum compromise between ensuring clear-sky pixels and keeping a large number of data points. Similarly, a value between 60° and 70° is recommended for the solar zenith angle cutoff. Apart from these restrictions, there are studies that have shown that the noise level in the SO₂ column is rather large during the winter months, even at middle latitudes as those of China (Fioletov et al., 2013). As a result, winter months are entirely excluded from their analyses, in particular when the end aim is the extraction of new, top-down emission databases.

In the following daily satellite observations were gridded onto monthly 0.25° × 0.25° fields and then onto seasonal and yearly maps. We first present the effect of spatially smoothing the SO₂ fields using seasonally averaged map from the GOME2/MetopA, hereafter GOME2A, data for year 2011. In Fig. 1 the seasonal mean SO₂ load is shown with cloud fraction of <0.2 and SZA <70° restrictions applied. The simple mean SO₂ load is shown alongside the smoothed SO₂ field is displayed. In the simple mean the gridded field was created by assigning the mean of all SO₂ satellite

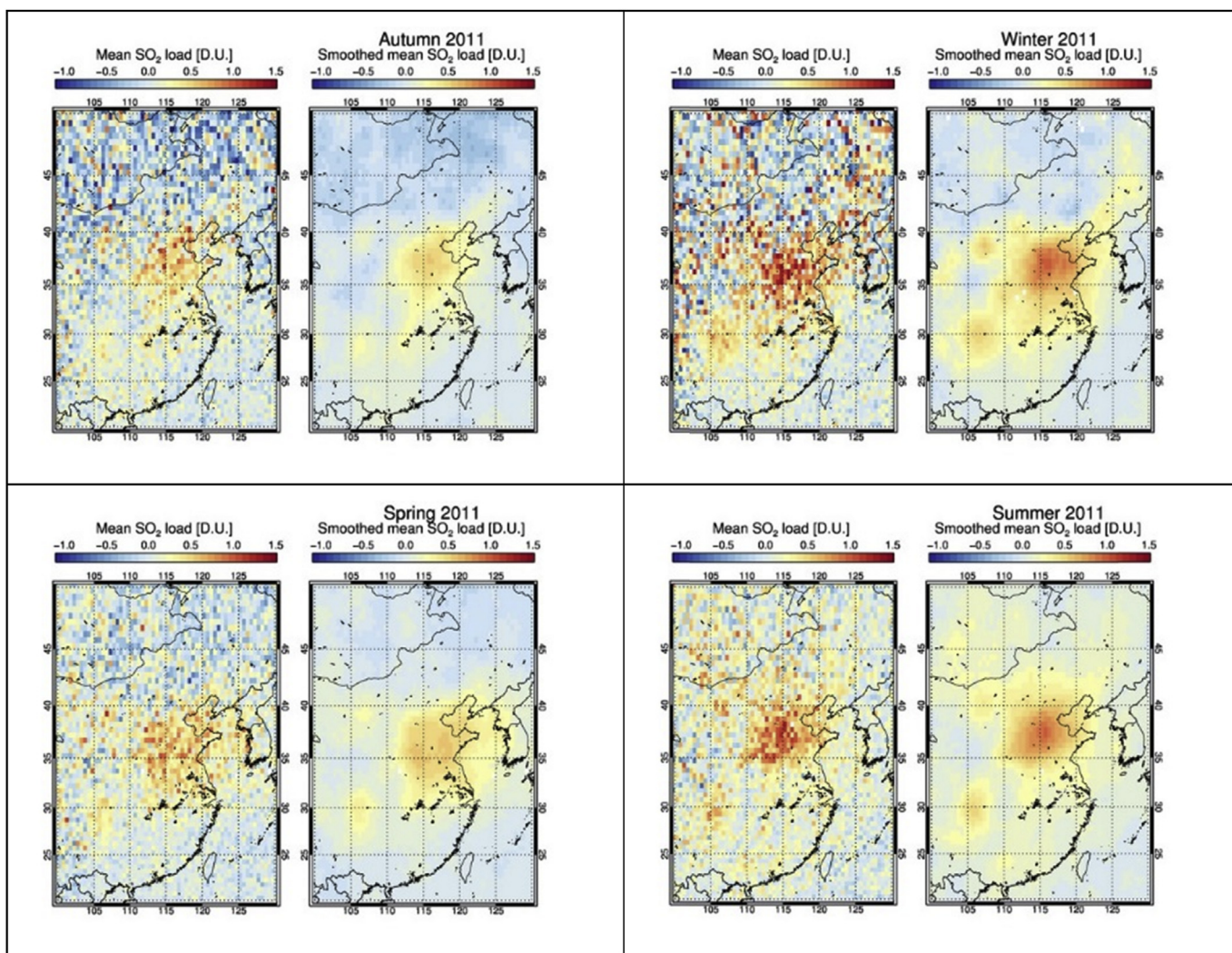


Fig. 1. Seasonal mean SO₂ loads [left panels] and smoothed mean SO₂ loads [right panels] for the GOME2/MetopA product in autumn [top left], winter [top right], spring [bottom left] and summer [bottom right] are shown.

observations whose central pixel falls within that $0.25 \times 0.25^\circ$ grid box. For the creation of the monthly and yearly gridded sets, the standard deviation, STD, is also used as a weight for the averaging process. In the smoothed SO_2 mean field, the SO_2 load assigned to each of the $0.25 \times 0.25^\circ$ boxes has been weighted by the SO_2 load of the eight surrounding cells. This way the noise levels, potential gridding issues, as well as gaps in the gridded set, have been averaged out, since the smoothing is applied to a running $0.75 \times 0.75^\circ$ domain.

One striking feature shown very explicitly by Fig. 1 is the fact that by spatially smoothing the mean GOME2A SO_2 values, the noise seen in the left panels of the composite figures entirely disappears in the right panels and known SO_2 hot-spots appear more clearly; the greater Beijing Area being one of them. A second point to note is that there appears not to be any difference between using only the cloud fraction or both the cloud fraction and the SZA as restrictions for the spring and summer months [not shown here]. This is not the case for the winter months, where effectively the simple mean gridded SO_2 product is far too noisy [with STDs higher than 5 D.U.] and the domain coverage is severely reduced when applying the SZA restriction as well. We hence recommend that, depending on the intended use of these datasets, great attention is given to the data filters applied.

For presenting the satellite observations, and to avoid repetitious discussions, the strict restriction for a $\text{clf} < 0.2$ and a $\text{SZA} < 70^\circ$ will be shown on yearly fields. Year 2011 was chosen for all cases (Fig. 2). Due to the SCIAMACHY revisit time, the number of pixels per grid box is smaller than for GOME2 as well as than in the OMI

fields [not shown here]. Even though the number of negative SO_2 levels for SCIAMACHY is high, producing a very noisy map, when applying spatial averaging the hot spots emerge strongly. For the OMI observations, due to their high spatial resolution, the associated standard deviation is quite low, usually below 1 D.U. and the number of observations per grid box may approach values higher than 20–25, especially for the summer months [not shown here.] Another point to note is that the SO_2 fields for both the NASA and the BIRA algorithms given by the simple mean and by the smoothed mean do not differ as much as the equivalent ones for the other two sensors, again due to the small OMI pixel size. In the yearly maps presented in Fig. 2, for demonstrational purposes, both regional and point SO_2 sources are revealed.

3.2. Point sources

The list of power plants in the People's Republic of China, PRC, considered in this work is given in Appendix I. The list of megacities in China considered in this work are given in Appendix II. This lists do not form a final enumeration of possible anthropogenic SO_2 sources around China; however, a fair number of the most known power plants and industrial regions do appear here, as also in the works of Fioletov et al., 2016. In the recent work of McLinden et al., 2016, they estimated that around 10% of SO_2 sources revealed by satellite observations on a global scale are not included in the leading emission catalogues, further strengthening the case for the ability of space-borne instruments to robustly identify emitting locations.

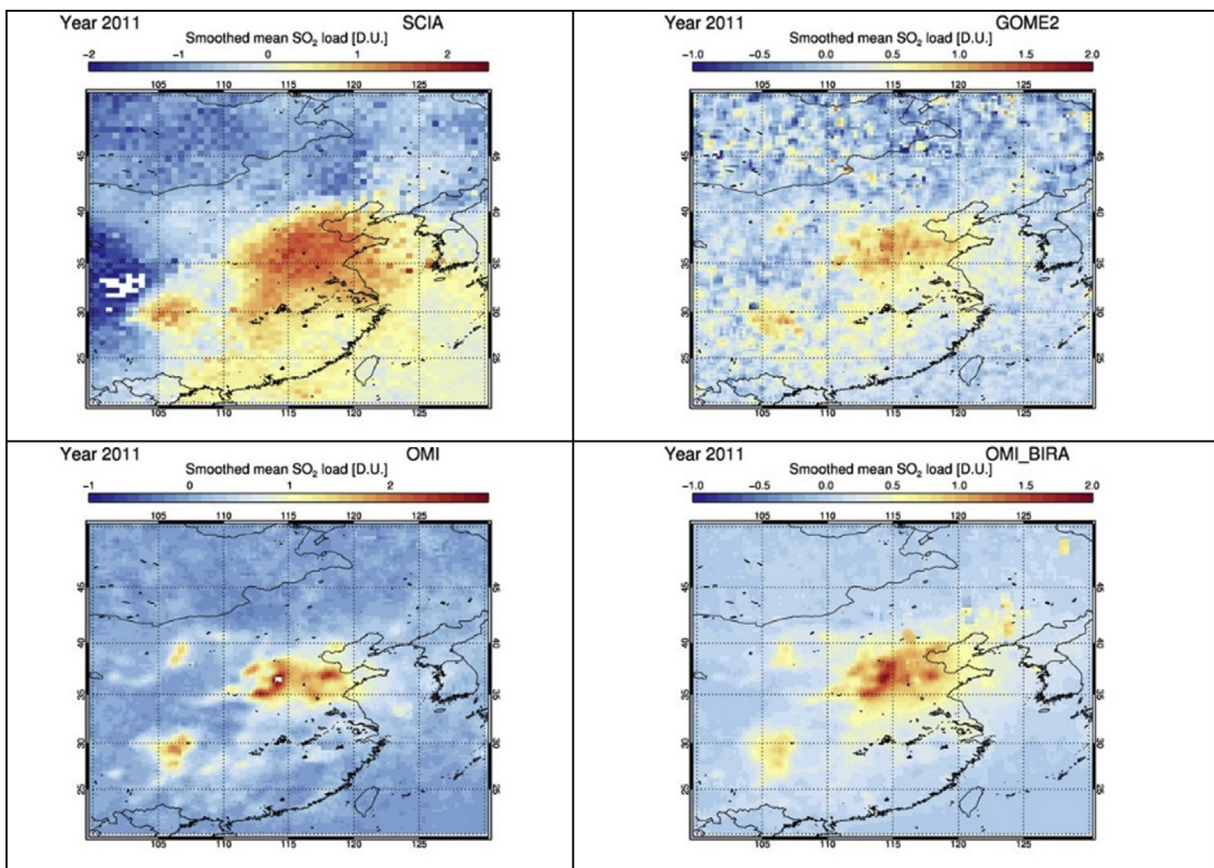


Fig. 2. Yearly smoothed SO_2 load [D.U.] over Eastern China in 2011. **Upper left:** SCIAMACHY/Envisat; **upper right:** GOME2/MetopA; **lower left:** OMI_NASA/Aura and **lower right:** OMI_BIRA/Aura. Not the slightly altered colour scale to accommodate the different SO_2 load ranges. (For interpretation of the references to colour in this figure legend, the reader is referred to the web version of this article.)

In Fig. 3 the locations of the known point SO₂ sources listed in Appendix I and Appendix II are shown superimposed on GOME2A maps for year 2011. The clarity of the loading when viewing the smoothed gridded map is promising for the analysis of these point sources. Note also that there undoubtedly exist more SO₂ sources in China which have not been identified in this work and are hence beyond the scope of this discussion.

In the following section, the findings of the point sources analysis are presented via time series and trend analysis.

3.3. Monthly mean time series analysis

The monthly mean time series for the locations examined were extracted from the $0.25^\circ \times 0.25^\circ$ gridded monthly mean data created for a $5^\circ \times 5^\circ$ degree box around each point source. Then, using spherical trigonometry and allowing a 40 km radius of search between the site and the gridded monthly mean fields, monthly mean estimates for each point source and each of the satellite sensors were calculated. Apropos, different radii of search were examined, such as 20 km and 60 km, but it was found that in order to keep the uniformity in investigation between the different sensors, the 40 km radius was the optimal choice. Please note at this stage that, unavoidably, due to the different time spans of the missions, the time series analysis is performed on a different time frame for each of the three instruments. Hence, the SCIAMACHY time series spans from 2004 to 2011, the OMI time series from 2005 to 2014 and the GOME2A time series from 2007 to 2014.

As will be shown later on, outliers in the monthly mean time series were found to affect the linearly regressed trend lines fit to the data for each location [see Fig. 4]. Moreover, we found that differences from the best-fit lines were not normally-distributed and were strongly skewed. This was particularly the case at the sites affected by strong seasonality in the SO₂ load or sporadic changes in the aerosol load. As a result, we opted to filter out outliers using statistics associated with the median rather than the mean. Monthly mean values that were found to be higher than 1.5 times the inter-quartile range (IQR) or below 1.5 times the IQR were flagged and excluded [see Fig. 4]. The linear regression was then repeated excluding these values and the null hypothesis was tested with a two-tail *t*-test at the 95% level of significance. Hence, in the following, a statistically significant positive or negative trend is

reported when the associated *p*-value is less than 0.05. Furthermore, in order to ascertain the representativity of the time series, a minimum of 30 monthly mean values was permitted for the analysis, with locations left with less than 30 monthly mean points excluded from further discussion.

An example of a location with an important negative trend is shown in Fig. 4 via the monthly mean time series for the city of Dongguan. The monthly mean SO₂ loading calculated using a radius of 40 km based on the smoothed mean gridded fields unfiltered for outliers and filtered for outliers is given. Dongguan is a prefecture-level city of approximately 6.5 million inhabitants in central Guangdong province, China. Dongguan, an important industrial city located in the Pearl River Delta, borders with the provincial capital of Guangzhou to the North, Huizhou to the Northeast, Shenzhen to the South, and the Pearl River to the West. It is part of the Pearl River Delta megacity with more than 45 million inhabitants at the 2010 census spread over nine municipalities (including Macao) across an area of 17,573 km². A strong as well as statistically significant negative trend has been identified for the filtered time series based on the area weighed mean SO₂ grid for GOME2A, OMI_NASA and OMI_BIRA [discussed further below]. Numerous points may be made based on this composite Figure; firstly that the variability of the monthly mean values reduces almost by a factor of 10 when using the smoothed mean grid as input for all sensors and algorithms instead of the simple mean gridded fields [not shown here]. Then, in the specific example shown, the actual drift remains of the same order of magnitude and sign for the statistically significant cases, whereupon it can be seen that GOME2A [Fig. 4, first row, right], even though it has a larger footprint than OMI, does provide a very similar monthly mean variability as the OMI algorithms and OMI_BIRA in particular [Fig. 4, bottom row, right]. Conversely, it has become apparent that the SCIAMACHY dataset is affected by many gaps in the time series due to its footprint and revisiting times, as well as higher levels of noise in the data, as attested to by the magnitude of the associated STD. As a result, for the example case of Dongguan, applying the outlier filter decreases the amount of data by such a large amount that no trend analysis may be further applied. This result was found for numerous of the locations chosen, even more so at the high latitudes where the SZA and *clf* restrictions all but excluded entire regions from SCIAMACHY analysis.

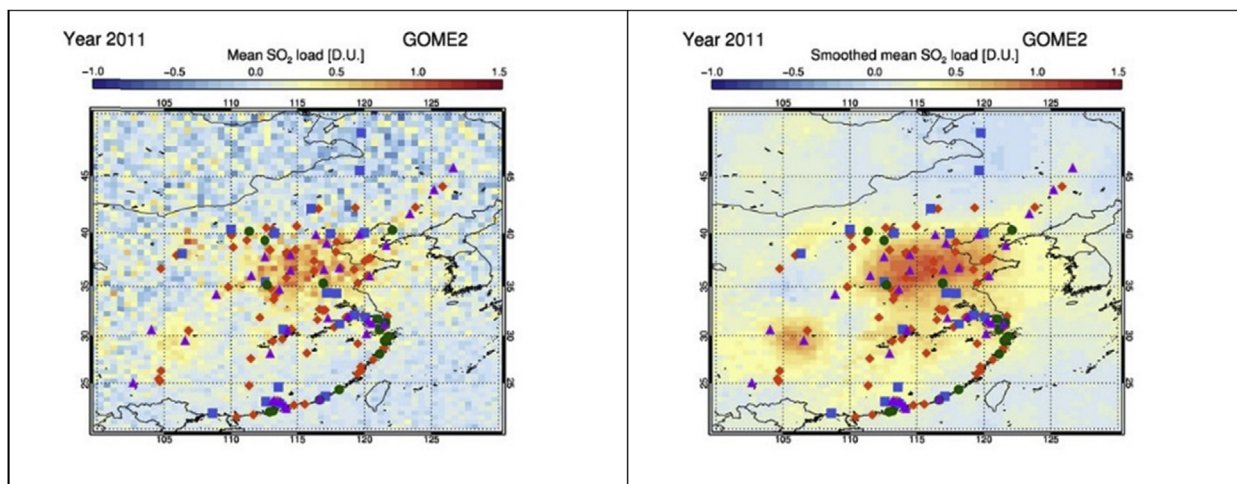


Fig. 3. The locations of the SO₂ point sources listed in Appendix I and Appendix II are shown; in orange diamonds power plants with capacity less than 2200 MW; in blue squares, power plants with capacity between 2200 and 3500 MW and in green circles the power plants with capacity higher than 3500 MW. The purple triangles denote the Chinese megacities examined. **Left:** the simple mean SO₂ load for year 2011 from GOME2A. **Right:** the smoothed mean SO₂ load for year 2011. (For interpretation of the references to colour in this figure legend, the reader is referred to the web version of this article.)

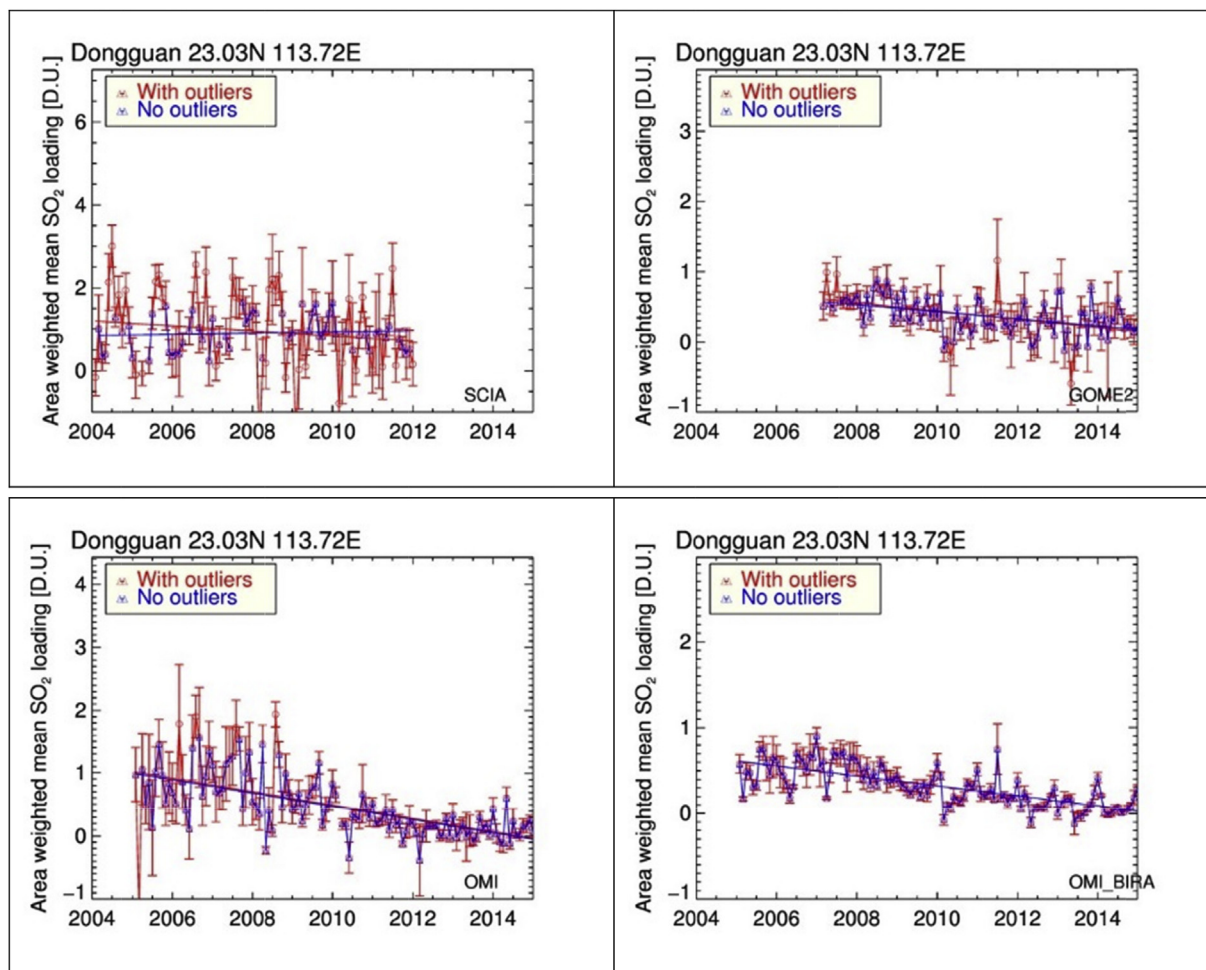


Fig. 4. The monthly mean time series for the city of Dongguan as observed by the SCIAMACHY sensor [top left], GOME2A [top right], OMI_NASA [bottom left] and OMI_BIRA [bottom right.] The monthly mean SO₂ loading calculated based on the smoothed mean gridded fields is shown unfiltered for outliers [red] and filtered for outliers [blue]. (For interpretation of the references to colour in this figure legend, the reader is referred to the web version of this article.)

The effect of the choice of spatial averaging and filtering on the time series and trends calculated for the locations around China are given in Table 1. The numbers of the table depict the amount of locations [out of an original sample of 149] that fulfil each criterion stated given for the three algorithms in sequence: GOME2A, OMI_BIRA and OMI_NASA. In the first row, the statistical analysis is performed on the unfiltered simple mean SO₂ overpass time series. In the second row, on the filtered simple mean SO₂ overpass time series. In the third row, on the unfiltered area averaged mean SO₂ overpass time series and in the fourth row, on the filtered area averaged mean SO₂ overpass time series. Recall that by filtered, we refer to the monthly mean time series that the statistical exclusion of the $\pm 1.5 \times \text{IQR}$ was applied to all values and the outliers are excluded from the analysis. Also recall that this analysis is performed for ten full years for the OMI algorithms and for eight full years for GOME2A.

The first thing to note is that the application of the $N > 30$ criterion does not affect the amount of locations found for the two OMI algorithms as it does for the GOME2A datasets. Even with this simple exclusion, some 32 locations are excluded for GOME2A when applying this filter for the simple mean filtered SO₂ dataset and 22 for the area-weighted mean filtered SO₂ dataset. When further restricting the work by calculating the statistically significant cases the GOME2A dataset is left with between 17 and 47 locations, depending on the choice of monthly mean time series

whereas the two OMI datasets show a much larger amount of locations, between 70 and 102. Note how the amount of statistically significant locations increases for all satellite sets when employing the area-weighted average instead of the simple mean average, resulting from the noise levels in the individual datasets.

The vast majority of locations examined in this work show a statistically negative drift for the time spans examined per satellite lifetime [see final column of Table 1.] One might hence deduce that, as discussed in other works (van der A et al., 2016) the SO₂ emissions are by and large decreasing this past decade over different sites around China with few exceptions. Surprisingly enough, for the cases of positive drifts, the amount of locations with statistically significant ones increases when using the filtered monthly mean time series, a fact discussed further below as well. The trends for the locations discussed for the filtered area-weighted SO₂ monthly mean time series are shown in Fig. 5. Even though the colour scales for the two OMI algorithms are not the same, the locations of the significant SO₂ changes are very similar strengthening the case that these represent locations where the SO₂ emissions have decreased [or increased for 3–4 locations only] in the decade 2004 to 2014 inclusive.

Since numerous recent literature studies have shown a marked decline in the SO₂ levels in Eastern China from years 2010–2011 [for e.g. Krotkov et al., 2016 and references therein], the trend calculations summarized in Table 1, were repeated for years

Table 1
 The amount of locations that fulfil different criteria for GOME2A (first block), OMI_BIRA (second block) and OMI_NASA (third block). First column: the amount of locations whose monthly mean time series contain more than 30 points. Second column: as per first, for the statistically significant cases. Third column: as per second, separated into the amounts of positive and negative drifts. Fourth column: as per third, separated into the amounts of power plants and megacities. The differences in the row statistics are discussed in the text.

GOME2A (2007–2014)	N > 30	N > 30, Significance level > 95%	N > 30, Significance level > 95% positive drift negative drift		N > 30, Significance level > 95% Power Plant Cities	
Simple mean			1	16	9	8
With outliers	149	17				
Simple mean			2	21	15	8
No outliers	117	23				
Smoothed mean			1	31	18	14
With outliers	149	32				
Smoothed mean			4	43	34	13
No outliers	127	47				
OMI_BIRA (2004–2014)						
Simple mean	149	94	1	93	73	21
With outliers						
Simple mean	147	81	3	78	66	15
No outliers						
Smoothed mean	149	102	1	101	80	22
With outliers						
Smoothed mean	149	88	4	84	65	23
No outliers						
OMI (2004–2014)						
Simple mean	149	92	2	90	66	26
With outliers						
Simple mean	143	70	2	68	49	21
No outliers						
Smoothed mean	149	95	2	93	73	22
With outliers						
Smoothed mean	144	76	3	73	55	21
No outliers						

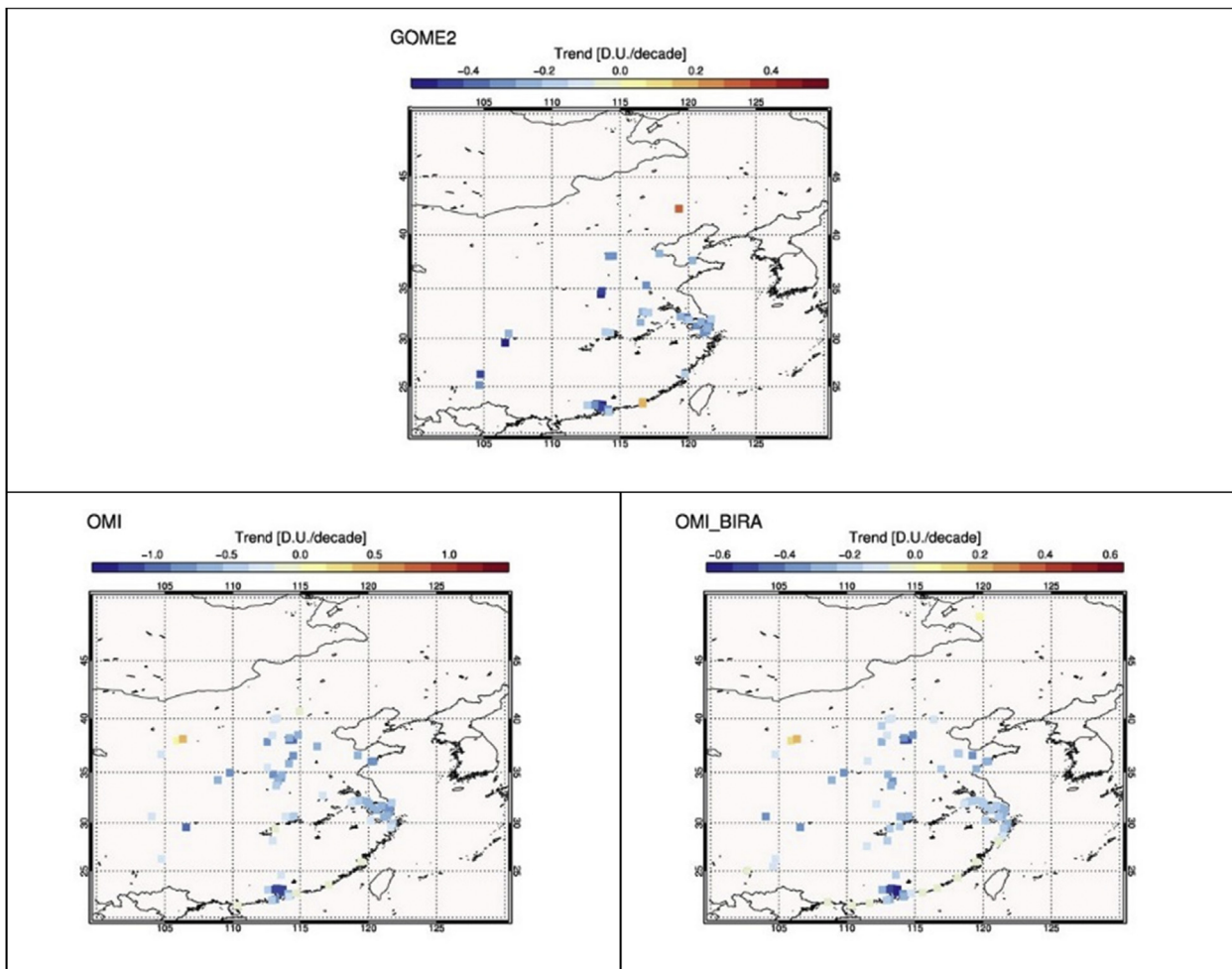


Fig. 5. The statistically significant trends in D.U. per decade for the GOME2A data [first row], the OMI_NASA data [second left] and the OMI_BIRA data [second right.] Note the colour scales do not span the same data range.

Table 2

The amount of locations for 2011–2014 period that fulfil different criteria for GOME2A (first), OMI_BIRA (second) and OMI_NASA (third). First column: the amount of locations whose monthly mean time series contain more than 30 points. Second column: as per first, for the statistically significant cases. Third column: as per second, separated into the amounts of positive and negative drifts. Fourth column: as per third, separated into the amounts of power plants and megacities.

GOME2A (2011–2014)	N > 30	N > 30, Significance level > 95%	N > 30, Significance level > 95% positive drift negative drift	N > 30, Significance level > 95% Power Plant Cities
Smoothed mean No outliers	98	23	2	21
OMI_BIRA (2011–2014) Smoothed mean No outliers	137	62	–	62
OMI (2011–2014) Smoothed mean No outliers	111	51	2	49
				42
				9

Table 3

Locations with a positive statistically significant drift for the GOME2A, OMI_NASA and OMI_BIRA datasets.

Sensor/algorithm	Location	Drift [D.U. per decade]	Standard deviation	Significance level [%]
GOME2A (2007–2014)	Haimeng	0.14	0.058	98.36
	Yuanbaoshan	0.28	0.098	99.43
	Shantou	0.17	0.069	98.63
	Urumqi	0.20	0.072	99.09
OMI_NASA (2005–2014)	Daba	0.099	0.035	99.51
	Lingwu	0.21	0.047	100
	Yimin	0.032	0.016	95.66
	Urumqi	0.079	0.026	99.72
OMI_BIRA (2005–2014)	Daba	0.17	0.061	99.35
	Lingwu	0.38	0.09	99.99
	Urumqi	0.16	0.061	98.79

2011–2014 included. The case of the smoothed gridded data excluding the outlier months from the statistics is shown in Table 2. As expected, most of the locations constantly provide a negative drift in the SO₂ load, whereas the positive drifts also remain. As mentioned above, the locations chosen for further study form by no means a complete catalogue; it should however be noted that in most published works, entire provinces are averaged and yearly trends presented [for e.g. see van der A et al., 2016], which might also account for the fact that the signal from new point sources, such as new power plants/industrial compounds, is averaged out.

Ground-based air quality observing stations also testify to the SO₂ decreasing trends around China and should be quoted here: Liang et al., 2014, report declining SO₂ levels for the Beijing-Tianjin-Shijiazhuang region; Zhu et al., 2015 for Wuhan city, whereas even an atmospheric background station in North China (Bai et al., 2015) also shows this general clearing up of the air over China.

4. Identifying special cases of SO₂ loading over China

4.1. Positive SO₂ changes

One of the main interesting results of this work was the identification of locations where the SO₂ load increased within the years studied. These locations are a mixture of megacity and power plant locations [Appendix I]. In Table 3 these locations are enumerated for the three datasets. These locations are also depicted in Fig. 6. The difference in locations observed between the GOME2A and OMI sensors may be partially due to the degradation of the former instrument (Dikty et al., 2011); the Haimeng Power Plant, in Guangdong Province is very near to the city of Shantou, which of course decreases the amount of independent locations showing a positive trend for the entire time span.

Some of these locations, also show an interesting spring-time feature. In Fig. 7 two such sites are presented; Lingwu is the most important industrial city of the Ningxia Hui Autonomous Region, in

the northwestern region of the People's Republic of China. However, Ningxia is the province with the third smallest gross domestic product in China, even though its neighbors, Inner Mongolia and Shaanxi, are among the strongest emerging provincial economies in the country. The positive trend observed by both OMI algorithms, shown in Fig. 7, left, may be in effect identifying possible industrial growth of the city. Several big power plants are also currently being built/upgraded in Ningxia¹ which would explain the increase in SO₂ observed by the satellite sensors [see also van der A et al., 2016 and references therein]. A second interesting feature of this Figure are the high SO₂ estimates for the spring months, also observed in higher frequency in Fig. 7, right, where the time series of the city of Ürumqi, the capital of the Xinjiang Uyghur Autonomous Region also in Northwest China is shown. When the spring-time outliers are excluded automatically by the outlier detection code, the positive trend remains, and in the case of Lingwu, it doubles. An obvious explanation for the behaviour of the time series of the twenty locations affected by this spring-time event is that we are faced with algorithm artefacts in the AMF calculation. However, a more daring possibility is that we might be observing Asian Dust transport. Also known as yellow dust, it is a seasonal meteorological phenomenon which affects much of East Asia sporadically during the months of spring [for e.g. Han et al., 2015; Kim et al., 2016; Liu et al., 2016]. The dust originates in the deserts of Mongolia, northern China and Kazakhstan where high-speed surface winds and intense dust storms kick up dense clouds of fine, dry soil particles. These clouds are then carried eastward by prevailing winds and pass over China, North as well as parts of the Russian Far East. For e.g., to explain the high values observed in 2008 for Lingwu, Fig. 7, left, we might examine the March 2008 dust event when the characteristic “yellow dust” from the Gobi Desert blew eastward over the Beijing region, the Yellow Sea, and North and

¹ <http://www.ningdong.gov.cn/zcms/wwwroot/2014ywbzgnxndnyhgjd/investmentguide/partnerlist/287162.shtml>.

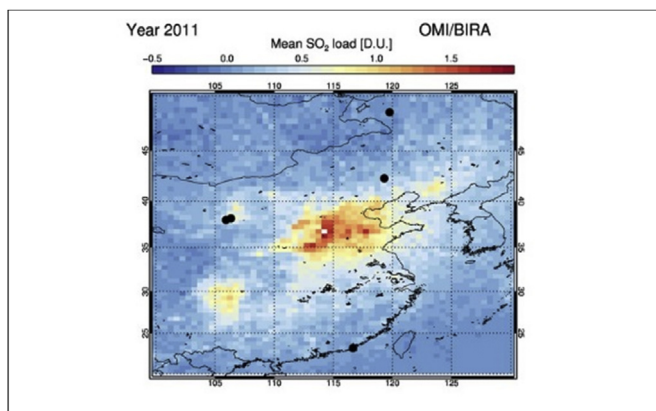


Fig. 6. The locations of the cities where positive trends were found by either of the satellite datasets are shown as black dots. The background field is the 2011 OMI_BIRA mean SO_2 load in D.U.

South Korea (Luo et al., 2014 and <http://earthobservatory.nasa.gov/IOTD/view.php?id=8477>). Extreme aerosol loading may hinder the AMF calculation, not in the sense of an artefact, but of a natural phenomenon not included in the radiative transfer calculations. The spring-time behaviour of the twenty locations is an issue currently under investigation.

4.2. Seasonality in SO_2 loading

For a significant number of the locations examined there appeared to be a strong and well-defined seasonality in the SO_2 signal, pointing to the possibility of a strong inter-annual variability observable from space. In Fig. 8 two such locations are shown as example; the city of Suzhou, in Jiangsu Province and a power plant in Yuenyang, in Yunnan Province.

Singular Spectrum Analysis (SSA) is a non-parametric spectral estimation technique based on time-delay embedding of a time series to decompose it into an additive sum of interpretable components [see for e.g. Golyandina et al., 2001; Ghil et al., 2002]. These components include the trend, possible periodicity and of course the noise in the original time series. A more generic and automated

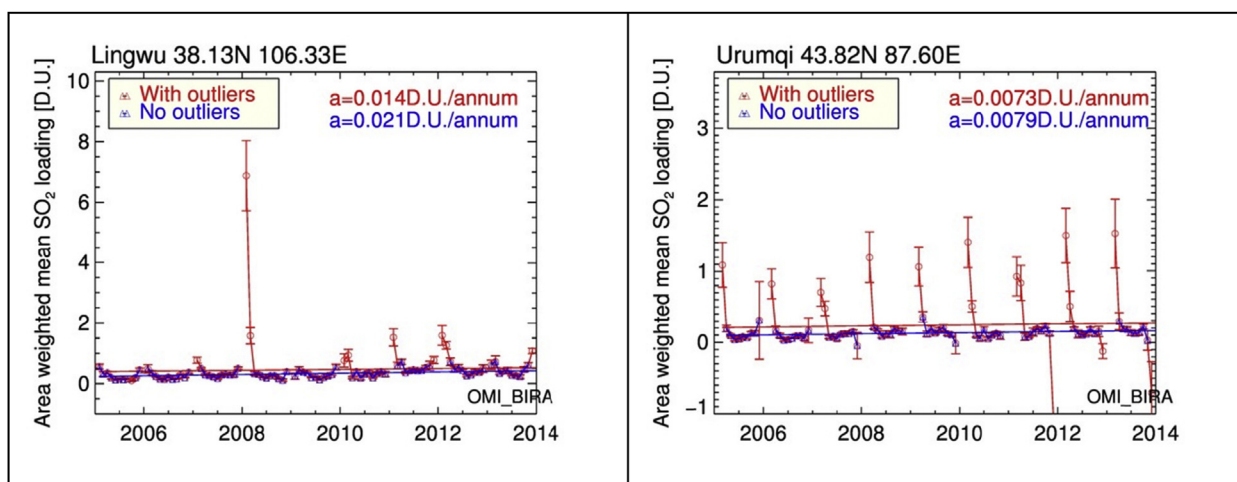


Fig. 7. Two interesting locations with positive trends and high spring-time signatures in the reported SO_2 load, the city of Lingwu, Ningxia Hui Autonomous Region, China [left] and Ürümqi, Xinjiang Uyghur Autonomous Region, China [right]. The format follows that of Fig. 4.

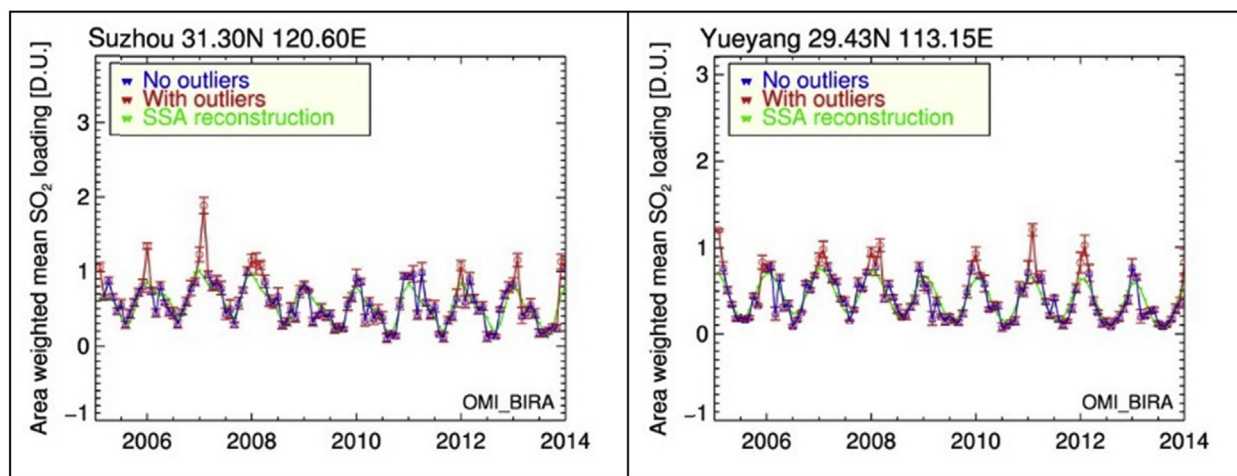


Fig. 8. Seasonal variability in the reported SO_2 load over the city of Suzhou, Jiangsu [left] and a power plant in Yuenyang, Yunnan [right]. The original monthly mean time series is shown in red; the time series excluding the outlier months as described in the text is shown in blue; the singular spectrum analysis reconstruction is shown in green. (For interpretation of the references to colour in this figure legend, the reader is referred to the web version of this article.)

system for the detection of both significant trends, as well as clear seasonal features, is being developed in Taylor et al. (2016a) where a Discrete Fourier Transform (DFT) analysis is also applied to the time series. This permits the actual extraction and quantification of the main temporal components as well as identification of statistically significant seasonal cycles. Parts of this work have already been presented in Taylor et al., 2016b. Fig. 9 shows the total trend, periodicity and noise components extracted by SSA from the interpolated time series at Suzhou and Yueyang; the pictorial explanation of the methodology behind the detection of statistically-significant annual and bi-annual cycles in each case is shown in the bottom row of Fig. 9.

The procedure used to identify statistically-significant cycles is briefly summarized as follows. We begin by subtracting the SSA nonlinear trend [shown as example in the upper panels of the top row of Fig. 9] to produce detrended time series. At this point, we also calculate the correlation coefficient, labeled $R(ols vs ssa)$ between a best fit linear line and the calculated SSA trend line

[penultimate column of Table 4]. The DFT is then computed to produce a Fourier line spectrum containing 192 frequencies in the range 0–0.5 cycles/month (i.e. at half the sampling frequency) as shown by the raw spectrum in Fig. 9 [bottom row, grey dots]. Although the SSA method is able to robustly extract the total periodicity and noise, it is unable to identify the sinusoidal components often associated with seasonal variability, i.e. the actual numbers of the periodicity; hence the need for the extra DFT calculation. In order to ascertain that the DFT is providing the same seasonality as the SSA, we calculate the correlation between the two methods, denoted as $R(dft vs ssa)$, [final column of Table 4]. To identify the statistically-significant frequencies (identified as pink filled circles, peaks, bottom row, Fig. 9) we smooth the raw spectra by iteratively applying a Daniell filter since this produces the most stable spectral estimate for a given bandwidth and allows 95% confidence intervals [pink lines, bottom row, Fig. 9] to be constructed (see Bloomfield, 2004: pp181–184). Finally, the area under the smoothed spectrum [blue line, bottom row, Fig. 9] is used to

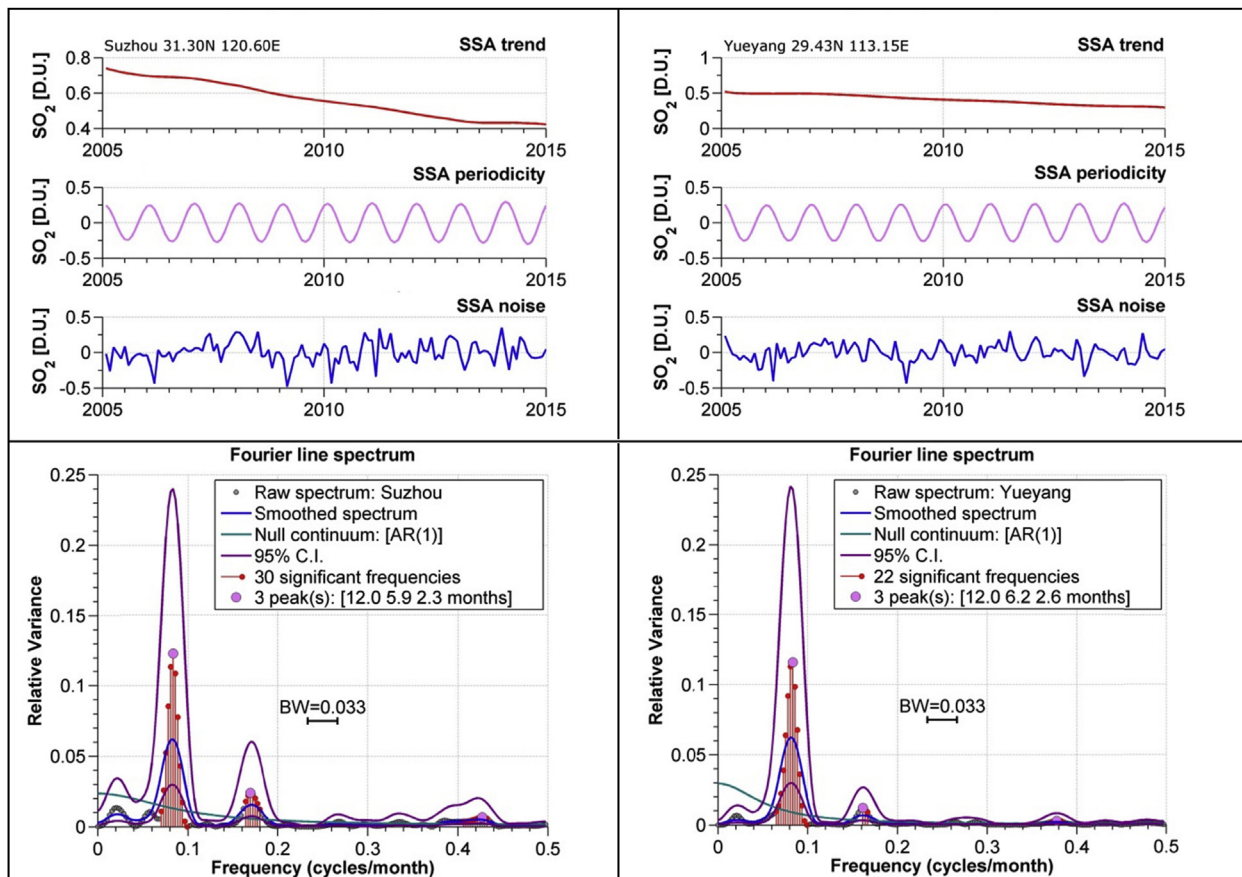


Fig. 9. [Upper panels] The total extracted trend, periodicity and noise SSA components for Suzhou (left) and Yueyang (right). [Lower panels] The detection of annual and bi-annual cycles (12 and 6 months respectively) using the method of Taylor et al. (2016a) for the SSA detrended time series at Suzhou (left) and Yueyang (right). The raw spectrum is given by the grey circles, the smoothed spectrum by the blue line, the null continuum by the green line, the 95% confidence interval (C.I.) by the purple line, the significant DFT frequencies by red circles and the actual peaks by pink filled circles. (For interpretation of the references to colour in this figure legend, the reader is referred to the web version of this article.)

Table 4

Summary statistics for detection of annual (12 ± 0.5 month), bi-annual (6 ± 0.5 month) and seasonal (3 ± 0.5 month) cycles at N sites in a sample of 141 cases studied that includes cities and power station locations. $R(ols vs ssa)$ is the mean correlation between the SSA trend and the ordinary least square regression fit, $R(dft vs ssa)$ being the mean correlation between the SSA and DFT periodicities.

Cycle Detected	N out of 141 cases analysed	%	$R(ols vs ssa)$	$R(dft vs ssa)$
Annual (12 month)	99	70.2	0.979	0.886
Bi-Annual (6 month)	60	45.4	0.962	0.713
Seasonal (3 month)	39	27.7	0.971	0.733

scale a first order auto-regressive AR(1) “red noise” model of the time series and produce the null continuum [green line, bottom row, Fig. 9]. A chi-squared test then flags up those statistically-significant frequencies whose spectral estimate (lower confidence interval, C.I.) is above the null continuum at the 95% level [red line and dots, bottom row, Fig. 9]. Peak frequencies are then given by the local maxima [pink filled circles, bottom row, Fig. 9]. Hence, we note that at both Suzhou and Yueyang, two statistically significant annual (12-month) and bi-annual (6-month) cycles are detected. In Table 4 we summarize the results of applying this seasonality detection scheme to a sample of outlier-removed time series at 141 locations from this study.

Annual and inter-annual SO₂ cycles are clearly evident in the monthly mean time series and at many of the locations examined in this work, see auxiliary material to this work in: <http://users.auth.gr/mariliza/China/>. All graphs depicting the main steps of the methodology described above are provided for each of the locations discussed in this paper. The seasonality is a strong component of the data and this variability is discoverable from space with the appropriate statistical tools, such as those briefly described in Taylor et al., 2016b, and fully deployed in Taylor et al., 2016a.

5. Short summary

The ability of the SCIAMACHY/Envisat, OMI/Aura and GOME2/MetopA satellite instruments, analysed by both operational and scientific algorithms, to observe the anthropogenic SO₂ load over China has been studied in this work. The optimal spatiotemporal, as well as filtering, choices required to attain a satisfactory signal-to-noise ratio for each sensor have been discussed, followed by an extensive monthly mean time series analysis on point locations, instead of province mean loads. In short:

- Irrespective of the instrument's pixel size, the recommended flagging restrictions of the operational algorithms do not permit a noise-free monthly mean map to be created for scientific purposes. A careful gridding and smoothing technique is paramount in order to obtain statistically significant monthly mean time series for locations of interest.
- For SO₂ emitting locations with a high enough SO₂ load, it is within the ability of the OMI/Aura measurements to provide a robust time series including the winter months, which are of high interest.
- Negative trends over more than 90% of the megacities and power plant sites examined in this work were revealed by both the GOME2/MetopA and the OMI/Aura observations.
- Positive trends for a few locations were also found for the decade 2005–2014 which remained statistically significant when limiting the time period to 2010–2014, the five years when most of the known power plants applied desulphurisation filters in their facilities. This finding impresses the need to not only focus SO₂ load studies on the provincial level, but also to

focus on emerging economies within the Chinese realm which introduce new industrial and power plant parks.

- A clear annual cycle in the SO₂ observed by the OMI/Aura instrument was unveiled, with highs in winter and lows in summer. Over 70% of the locations evaluated in this work showed this clear signal, which has been fully analysed and enumerated using a new state-of-the-art mathematical tool.
- A number of the locations studied have exhibited a strong and repetitive signal in the reported SO₂ load over spring months; this fact merits further study as these spring-time highs might be possible outcomes of Gobi Desert dust intrusions that hinder the capabilities of the satellite algorithms, after a fashion.

As also shown in the work of van der A et al., 2016, when a strict control by the Chinese authorities on the actual use of the desulphurisation installations was enforced around 2007–2008, a clear effect on the air quality was observed by both ground- and space-born instruments. In the last couple of years, the effect of the new restrictions on NO_x emissions from heavy industry and power plant regulations is gradually revealed by satellite observations as well. It hence follows that enforcing and updating current legislation and measures will certainly clean up the air over China, as was achieved for Europe in the last two decades [European Environmental Agency; <http://www.eea.europa.eu/>.]

As future steps, we consider that the wealth of sulphur dioxide emissions information obtainable from satellite observations can be used in top-down emission inventory calculations to update the more traditional bottom-up inventories and hence permit a global well of information on the atmosphere sulphur dioxide load from anthropogenic sources.

Acknowledgements

The authors would like to acknowledge; the EU FP7 MarcoPolo/Panda project, <http://www.marcopolo-panda.eu/> under agreement No 606953, FP7-SPACE-2013, European Commission Research Executive Agency (REA), the EUMETSAT Satellite Application Facility for Atmospheric Composition and UV Radiation O3MSaf project, <http://o3msaf.fmi.fi/>, and the NASA Goddard Earth Sciences (GES) Data and Information Services Center (DISC) Mirador service, <http://mirador.gsfc.nasa.gov/>.

Appendix A. Expected locations of detectable SO₂ emissions in China.

Appendix I. The list of power plants in the People's Republic of China considered in this work sorted by the reported capacity in MW in 2010. List adapted from https://en.wikipedia.org/wiki/List_of_power_stations_in_China#Coalas well as <http://carma.org/plant>

Power plant	Province	Capacity [MW]	Latitude	Longitude
Tuoketuo	Neimenggu	5400	40°11'49"N	111°21'52"E
Beilun	Zhejiang	5000	29°56'26"N	121°48'48"E
Jiaxin	Zhejiang	5000	30°37'47"N	121°08'46"E
Taishan	Guangdong	5000	21°52'00"N	112°55'22"E
Waigaoqiao	Shanghai	5000	31°21'21"N	121°35'50"E
Yingkou	Liaoning	4840	40°18'17"N	122°06'17"E
Yangcheng	Shanxi	4620	35°28'11"N	112°34'41"E
Qinbei	Henan	4400	35°10'11"N	112°42'56"E
Ninghai	Zhejiang	4400	29°29'16"N	121°30'34"E
Zouxian	Shandong	4400	35°19'36"N	116°56'02"E
Houshi	Fujian	4200	24°18'11"N	118°07'35"E

(continued)

Power plant	Province	Capacity [MW]	Latitude	Longitude
Nantong	Jiangsu	4060	31°45'25"N	120°58'31"E
Yuhuan	Zhejiang	4000	28°06'57"N	121°08'16"E
Jianbi	Jiangsu	3980	32°10'54"N	119°34'35"E
Shajiao	Guangdong	3880	22°44'50"N	113°40'39"E
Zhujiang	Guangdong	3800	22°48'51"N	113°34'04"E
Shangdu	Inner Mongolia	3720	42°13'27"N	116°01'41"E
Datong_II	Shanxi	3720	40°01'44"N	113°17'37"E
Shidongkou	Shanghai	3600	31°27'49"N	121°24'15"E
Suizhong	Liaoning	3600	40°04'48"N	120°00'27"E
Xuzhou	Jiangsu	3460	34°23'10"N	117°15'28"E
Wuhu_Huadian	Anhui	3320	31°14'22"N	118°09'06"E
Pengcheng	Jiangsu	3280	34°22'40"N	117°10'35"E
Lingwu	Ningxia	3200	38°08'54"N	106°20'45"E
Qinzhou	Guangxi	3200	21°42'50"N	108°36'53"E
Shaoguan	Guangdong	3200	24°35'03"N	113°35'00"E
Hanchuan	Hubei	3200	30°39'22"N	113°55'23"E
Xutang	Jiangsu	3200	34°20'55"N	117°55'55"E
Huilai	Guandong	3200	23°00'20"N	116°32'48"E
Sanbaimeng	Guandong	3200	23°33'58"N	117°05'49"E
Dalate	Inner Mongolia	3180	40°22'00"N	109°59'45"E
Hongjun	Inner Mongolia	3000	45°30'26"N	119°39'00"E
Changshu	Jiangsu	3000	31°45'25"N	120°58'31"E
Tongling	Anhui	2975	30°53'30"N	117°45'00"E
Taicanggang	Jiangsu	2770	31°35'05"N	121°15'25"E
Fuzhou	Fujian	2720	25°59'27"N	119°28'54"E
Lusigang	Jiangsu	2640	32°03'31"N	121°43'34"E
Jiutai	Jilin	2640	44°9'4"N	125°50'20"E
Shangan	Hebei	2620	38°03'25"N	114°11'46"E
Xinmi	Henan	2600	34°29'55"N	113°35'46"E
Puqi	Hubei	2600	29°39'52"N	113°52'23"E
Ligang	Jiangsu	2600	31°56'22"N	120°04'54"E
Zhuhai	Guangdong	2600	21°58'04"N	113°10'56"E
Yueyang	Hunan	2525	29°26'47"N	113°09'31"E
Pucheng	Shaanxi	2520	34°58'42"N	109°47'56"E
Datong_Tashan_Pithead	Shaanxi	2520	39°55'35"N	113°05'01"E
Fengzhen	Inner Mongolia	2520	40°24'18"N	113°08'47"E
Dingzhou	Hebei	2520	38°30'50"N	114°50'41"E
Shanwei	Guangdong	2520	22°42'21"N	115°33'17"E
Liuan	Anhui	2520	31°40'03"N	116°29'56"E
Fengtai	Anhui	2520	32°45'26"N	116°39'00"E
Tianji	Anhui	2520	32°40'09"N	117°01'31"E
Huanghua	Hebei	2520	38°18'36"N	117°52'43"E
Changzhou	Jiangsu	2520	31°57'30"N	119°59'33"E
Yueqing	Zhejiang	2520	28°10'15"N	121°05'26"E
Dezhou	Shandong	2520	37°27'07"N	116°14'35"E
Ningde	Fujian	2520	26°45'27"N	119°44'13"E
Pannan	Guizhou	2400	25°28'08"N	104°35'30"E
Diandong	Yunnan	2400	25°11'59"N	104°40'57"E
Faer	Guizhou	2400	26°19'31"N	104°46'11"E
Daba	Ningxia	2400	37°59'02"N	105°55'41"E
Hexi	Shaanxi	2400	39°49'22"N	110°02'04"E
Jinjie	Shaanxi	2400	38°44'10"N	110°10'01"E
Hequ	Shaanxi	2400	39°22'59"N	111°11'08"E
Jinzhushan	Zhejiang	2400	27°37'34"N	111°28'55"E
Yangxi	Guangdong	2400	21°32'15"N	111°40'13"E
Daihai	Inner Mongolia	2400	40°31'14"N	112°40'04"E
Liaocheng	Shandong	2400	36°29'21"N	116°14'35"E
Duolun	Inner Mongolia	2400	42°12'59"N	116°34'24"E
Lanxi	Zhejiang	2400	29°11'12"N	119°30'23"E
Tieling	Liaoning	2400	42°20'40"N	123°48'15"E
Fengcheng	Jiangxi	2400	28°11'45"N	115°42'31"E
Guangan	Sichuan	2400	30°31'41"N	106°49'34"E
Kemeng	Fujian	2400	26°22'24"N	119°45'44"E
Luohu	Anhui	2400	32°41'07"N	117°04'40"E
Pingliang	Gansu	2400	35°30'06"N	106°47'10"E
Pingwei	Anhui	2400	32°41'03"N	116°54'05"E
Wushashan	Zhejiang	2400	29°30'22"N	121°39'51"E
Xiangfan	Hubei	2400	31°54'57"N	112°10'10"E
Xibaipo	Hebei	2400	38°14'45"N	114°13'09"E
Yangluo	Hubei	2400	30°41'38"N	114°32'35"E
Yangzhou_II	Jiangsu	2400	32°16'12"N	119°25'19"E
Zhanjiang	Guangdong	2400	21°18'35"N	110°24'34"E
Xingdian	Shandong	2250	36°46'57"N	118°14'09"E
Shouyangshan	Henan	2240	34°43'53"N	112°45'21"E

(continued on next page)

(continued)

Power plant	Province	Capacity [MW]	Latitude	Longitude
Hebi	Henan	2200	35°51'04"N	114°10'44"E
Panshan	Tianjin	2200	39°58'55"N	117°27'40"E
Yimin	Neimenggu	2200	48°33'01"N	119°46'40"E
Huangpu	Guangdong	2170	23°04'43"N	113°29'44"E
Jingyuan	Gansu	2150	36°43'46"N	104°45'37"E
Yuanbaoshan	Neimenggu	2100	42°18'12"N	119°19'45"E
Hezhou	Guangxi	2090	24°44'15"N	111°21'09"E
Wujing	Shanghai	2075	31°03'31"N	121°27'56"E
Banqiao	Jiangsu	2070	31°56'52"N	118°37'49"E
Taizhou	Zhejiang	2070	28°41'53"N	121°27'28"E
Rizhao	Shandong	2060	35°20'40"N	119°30'40"E
Haimeng	Guangdong	2060	23°11'17"N	116°39'14"E
Pinghai	Guangdong	2060	22°36'32"N	114°44'34"E
Huangdao	Shandong	2050	36°02'18"N	120°13'10"E
Shuangyashan	Heilongjiang	2030	46°33'55"N	131°40'18"E
Yuzhou	Henan	2020	34°10'28"N	113°21'21"E
Dingxiang	Shaanxi	2000	38°28'22"N	112°57'25"E
Luyang	Henan	2000	34°49'15"N	113°00'51"E
Yaomeng	Henan	2000	33°44'14"N	113°14'23"E
Beijiang	Tianjin	2000	39°13'08"N	117°55'50"E
Jinling	Jiangsu	2000	32°10'18"N	119°01'07"E
Jurong	Jiangsu	2000	32°12'46"N	119°12'34"E
Weifang	Shandong	2000	36°38'37"N	119°13'58"E
Laizhou	Shandong	2000	37°25'56"N	120°01'05"E
Penglai	Shandong	2000	37°40'47"N	120°18'50"E
Nanshan	Shandong	2000	37°43'44"N	120°26'53"E
Cangnan	China	2000	27°29'54"N	120°39'44"E
Caojing	Shanghai	2000	30°45'36"N	121°23'59"E
Shentou_II	Shaanxi	2000	39°22'04"N	112°32'00"E
Taizhou	Jiangsu	2000	32°11'14"N	119°54'59"E

Appendix II. The list of megacities in the People's Republic of China considered in this work sorted by their reported metro area population based on the 2010 census. List adapted from: https://en.wikipedia.org/wiki/List_of_cities_in_China_by_population_and_built-up_area.

City	Province	Population [2010 census]	Latitude	Longitude
Shanghai	Shanghai	24800000	31°12'N	121°30'E
Beijing	Beijing	21150000	39°54'N	116°23'E
Guangzhou	Guangdong	12400000	23°08'N	113°16'E
Shenzhen	Guangdong	11700000	22°33'N	114°06'E
Tianjin	Tianjin	10600000	39°08'N	117°11'E
Shijiazhuang	Hebei	10163788	38°04'N	114°29'E
Chongqing	Chongqing	9977000	29°33'N	106°34'E
Handan	Hebei	9174683	36°36'N	114°29'E
Wuhan	Hubei	9158000	30°35'N	114°17'E
Dongguan	Guangdong	7280000	23°02'N	113°43'E
Hong Kong	Hong Kong	7200000	22°16'N	114°11'E
Chengdu	Sichuan	6670000	30°39'N	104°03'E
Foshan	Guangdong	6486000	23°01'N	113°07'E
Nanjing	Jiangsu	5866000	32°03'N	118°46'E
Harbin	Heilongjiang	5687000	45°45'N	126°38'E
Shenyang	Liaoning	5568000	41°48'N	123°24'E
Hangzhou	Zhejiang	5448000	30°15'N	120°10'E
Xian	Shaanxi	4975000	34°16'N	108°54'E
Zibo	Shandong	4530000	36°50'N	118°08'E
Linfen	Shanxi	4316612	36°05'N	111°31'E
Shantou	Guangdong	4175000	23°21'N	116°40'E
Zhenzhou	Henan	3964000	34°46'N	113°39'E
Qingdao	Shandong	3797000	36°04'N	120°23'E
Jinan	Shandong	3697000	36°40'N	116°59'E
Changchun	Jilin	3694000	43°54'N	125°12'E
Taiyuan	Shanxi	3495000	37°52'N	112°33'E
Kunming	Yunnan	3472000	25°04'N	102°41'E
Suzhou	Jiangsu	3463000	31°18'N	120°36'E
Wuxi	Jiangsu	3366000	31°34'N	120°18'E
Dalian	Liaoning	3359000	38°55'N	121°38'E
Changsha	Hunan	3335000	28°11'N	112°58'E
Urumqi	Xinjiang	3123000	43°49'N	087°36'E
Hefei	Anhui	3012000	31°52'N	117°17'E
Qinhuangdao	Hebei	2987605	39°56'N	119°36'E

References

- Bai, J.H., Wu, Y.M., Chai, W.H., Wang, P.C., Wang, G.C., 2015. Long-term variation of trace gases and particulate matter at an atmospheric background station in North China. *Adv. Geosciences* 5, 248–263. <http://dx.doi.org/10.12677/ag.2015.53025>.
- Bauduin, S., Clarisse, L., Clerbaux, C., Hurtmans, D., Coheur, P.-F., 2014. IASI observations of sulfur dioxide (SO₂) in the boundary layer of Norilsk. *J. Geophys. Res. Atmos.* 119, 4253–4263. <http://dx.doi.org/10.1002/2013JD021405>.
- Bloomfield, P., 2004. *Fourier Analysis of Time Series: An Introduction*. John Wiley & Sons. ISBN: 0-471-88948-2.
- Bogumil, K., Orphal, J., Homann, T., Voigt, S., Spietz, P., Fleischmann, O.C., Vogel, A., Hartmann, M., Bovensmann, H., Frerick, J., Burrows, J.P., 2003. Measurements of molecular absorption spectra with the SCIAMACHY pre-flight model: instrument characterization and reference data for atmospheric remote-sensing in the 230–2380 nm region. *J. Photochem. Photobiol. A* 157, 157–167.
- Bovensmann, H., Burrows, J.P., Buchwitz, M., et al., 1999. SCIAMACHY: mission objectives and measurement modes. *J. Atmos. Sci.* 56 (2), 127–150.
- Brión, J., Chakir, A., Daumont, D., Malicet, J., Parisse, C., 1993. High-resolution laboratory absorption cross section of O₃. Temperature effect. *Chem. Phys. Lett.* 213, 610–612.
- Carn, S.A., Yang, K., Prata, A.J., Krotkov, N.A., 2015. Extending the long-term record of volcanic SO₂ emissions with the ozone mapping and profiler suite nadir mapper. *Geophys. Res. Lett.* 42 <http://dx.doi.org/10.1002/2014GL02437>.
- Carn, S.A., Krueger, A.J., Krotkov, N.A., Gray, M.A., 2004. Fire at Iraqi sulfur plant emits SO₂ clouds detected by Earth Probe TOMS. *Geophys. Res. Lett.* 31 (19), 2–5. <http://dx.doi.org/10.1029/2004GL020719>.
- Carn, S.A., Krueger, A.J., Krotkov, N.A., Yang, K., Levelt, P.F., 2007. Sulfur dioxide emissions from Peruvian copper smelters detected by the Ozone Monitoring Instrument. *Geophys. Res. Lett.* 34 (9) <http://dx.doi.org/10.1029/2006GL029020>.
- De Foy, B., Krotkov, N.A., Bei, N., Herndon, S.C., Huey, L.G., Martínez, A.-P., Ruiz-Suárez, L.G., Wood, E.C., Zavala, M., Molina, L.T., 2009. Hit from both sides: tracking industrial and volcanic plumes in Mexico City with surface measurements and OMI SO₂ retrievals during the MILAGRO field campaign. *Atmos. Chem. Phys.* 9 (24), 9599–9617. <http://dx.doi.org/10.5194/acp-9-9599-16-2009>.
- Dikty, S., Richter, A., Weber, M., et al., 2011. GOME-2 on MetOp-A Support for Analysis of GOME-2 In-orbit Degradation and Impacts on Level 2 Data Products Final Report. Technical Document ITT 09/10000262, EUMETSAT, available at: http://www.eumetsat.int/website/wcm/idc/idcplg?IdcService=GET_FILE&dDocName=PDF_GOME2_MA_INORB_DEGR_L2_PRODS_REP&RevisionSelectionMethod=LatestReleased&Rendition=Web (last access: 21.04.16).
- Eisinger, M., Burrows, J.P., 1998. Tropospheric sulfur dioxide observed by the ERS-2 GOME instrument. *Geophys. Res. Lett.* 25 (22), 4177–4180. <http://dx.doi.org/10.1029/1998GL900128>.
- EUMETSAT, 2012. GOME-2/Metop-A Level 1B Product Validation Report No. 5: Status at Reprocessing G2RP-R2. Technical Document EUM/OPS-EPS/REP/09/0619, version 1F, EUMETSAT, available at: http://www.eumetsat.int/website/wcm/idc/idcplg?IdcService=GET_FILE&dDocName=pdf_gome_11b_prod_

- val&RevisionSelectionMethod=LatestReleased&Rendition=Web (last access: 21.04.16).
- Fioletov, V.E., McLinden, C.A., Krotkov, N., Li, C., Joiner, J., Theys, N., Carn, S., Moran, M.D., 2016. A global catalogue of large SO₂ sources and emissions derived from the Ozone Monitoring Instrument. *Atmos. Chem. Phys. Discuss.* <http://dx.doi.org/10.5194/acp-2016-417> (in review).
- Fioletov, V.E., McLinden, C.A., Krotkov, N., Moran, M.D., Yang, K., 2011. Estimation of SO₂ emissions using OMI retrievals. *Geophys. Res. Lett.* 38 (21) <http://dx.doi.org/10.1029/2011GL049402>.
- Fioletov, V.E., McLinden, C.A., Krotkov, N., Yang, K., Loyola, D.G., Valks, P., Theys, N., Van Roozendael, M., Nowlan, C.R., Chance, K., Liu, X., Lee, C., Martin, R.V., 2013. Application of OMI, SCIAMACHY, and GOME-2 satellite SO₂ retrievals for detection of large emission sources. *J. Geophys. Res. Atmos.* 118 (19), 11399–11418. <http://dx.doi.org/10.1002/jgrd.50826>.
- Ghil, M., Allen, M.R., Dettinger, M.D., Ide, K., Kondrashov, D., Mann, M.E., Robertson, A.W., Saunders, A., Tian, Y., Varadi, F., Yiu, P., 2002. Advanced spectral methods for climatic time series. *Rev. Geophys.* 40 (1), 1003. <http://dx.doi.org/10.1029/2000RG000092>.
- Golyandina, N., Nekrutkin, V., Zhigljavsky, A., 2001. *Analysis of Time Series Structure: SSA and Related Techniques*. Chapman and Hall/CRC.
- Gür, B., Spietz, P., Orphal, J., Burrows, J.P., 2005. *Absorption Spectra Measurements with the GOME-2 FMs using the IUP/IFE-UB's Calibration Apparatus for Trace Gas Absorption Spectroscopy*. CATGAS. Final Report, ESA/EUMETSAT.
- Han, Y., Wu, Y., Wang, T., Xie, C., Zhao, K., Zhuang, B., Li, S., 2015. Characterizing a persistent Asian dust transport event: optical properties and impact on air quality through the ground-based and satellite measurements over Nanjing, China. *Atmos. Environ.* 115, 304–316. <http://dx.doi.org/10.1016/j.atmosenv.2015.05.048>.
- Hassinen, S., Balis, D., Bauer, H., et al., 2016. Overview of the O3M SAF GOME-2 operational atmospheric composition and UV radiation data products and data availability. *Atmos. Meas. Tech.* 9, 383–407. <http://dx.doi.org/10.5194/amt-9-383-2016>.
- Khokhar, M.F., Frankenberg, C., Van Roozendael, M., Beirle, S., Kühl, S., Richter, A., Platt, U., Wagner, T., 2005. Satellite observations of atmospheric SO₂ from volcanic eruptions during the time-period of 1996–2002. *Adv. Space Res.* 36, 879–887.
- Kim, H.-S., Chung, Y.-S., Yoon, M.-B., 2016. An analysis on the impact of large-scale transports of dust pollution on air quality in East Asia as observed in central Korea in 2014. *Air Quality. Atmos. Health* 9 (1), 83–93. <http://dx.doi.org/10.1007/s11869-014-0312-5>.
- Klimont, Z., Smith, S.J., Cofala, J., 2013. The last decade of global anthropogenic sulfur dioxide: 2000–2011 emissions. *Environ. Res. Lett.* 8 (1), 014003. <http://dx.doi.org/10.1088/1748-9326/8/1/014003>.
- KNMI, 2012. Background Information about the Row Anomaly in OMI [online]. Available from: <http://www.knmi.nl/omi/research/product/rowanomaly-background.php> (accessed 5.08.15).
- Krotkov, N.A., McLinden, C.A., Li, C., Lamsal, L.N., Celarier, E.A., Marchenko, S.V., Swartz, W.H., Bucsela, E.J., Joiner, J., Duncan, B.N., Boersma, K.F., Veefkind, J.P., Levelt, P.F., Fioletov, V.E., Dickerson, R.R., He, H., Lu, Z., Streets, D.G., 2016. Aura OMI observations of regional SO₂ and NO₂ pollution changes from 2005 to 2015. *Atmos. Chem. Phys.* 16, 4605–4629. <http://dx.doi.org/10.5194/acp-16-4605-2016>.
- Krueger, A.J., 1983. Sighting of El Chichon sulfur dioxide clouds with the Nimbus 7 total ozone mapping spectrometer. *Science* 220 (4604), 1377–1379. <http://dx.doi.org/10.1126/science.220.4604.1377>.
- Lasnik, J., Stephens, M., Baker, B., et al., 2014. *Geostationary Environment Monitoring Spectrometer (GEMS) over the Korea Peninsula and Asia-Pacific Region*. American Geophysical Union. Fall Meeting 2014, abstract #A51A-3003, 2014AGUFM.A51A3003L.
- Lee, C., Martin, R.V., Van Donkelaar, A., Lee, H., Dickerson, R.R., Hains, J.C., Krotkov, N., Richter, A., Vinnikov, K., Schwab, J.J., 2011. SO₂ emissions and lifetimes: estimates from inverse modeling using in situ and global, space-based (SCIAMACHY and OMI) observations. *J. Geophys. Res. Atmos.* 116 (6) <http://dx.doi.org/10.1029/2010JD014758>.
- Li, C., Joiner, J., Krotkov, N. a., Bhartia, P.K., 2013. A fast and sensitive new satellite SO₂ retrieval algorithm based on principal component analysis: application to the ozone monitoring instrument. *Geophys. Res. Lett.* 40 (23), 6314–6318. <http://dx.doi.org/10.1002/2013GL058134>.
- Li, C., Zhang, Q., Krotkov, N.A., Streets, D.G., He, K., Tsay, S.-C., Gleason, J.F., 2010. Recent Large Reduction in Sulfur Dioxide Emissions from Chinese Power Plants Observed by the Ozone Monitoring Instrument, vol. 37, pp. 1–6. <http://dx.doi.org/10.1029/2010GL042594>.
- Liang, Z.Q., Ma, M.T., Du, G.F., 2014. Comparison of characteristics and trend analysis of atmospheric pollution in Beijing-Tianjin-Shijiazhuang during 2003–2012. *Air Pollut. Control* 32 (12), 78–81. http://en.cnki.com.cn/Article_en/CJFDTotal-HJGC201412020.htm.
- Liu, L., Huang, X., Ding, A., Fu, C., 2016. Dust-induced radiative feedbacks in north China: a dust storm episode modeling study using WRF-Chem. *Atmos. Environ.* 129 <http://dx.doi.org/10.1016/j.atmosenv.2016.01.019>.
- Lu, Z., Streets, D.G., De Foy, B., Krotkov, N.A., 2013. Ozone monitoring instrument observations of interannual increases in SO₂ emissions from Indian coal-fired power plants during 2005–2012. *Environ. Sci. Technol.* 47 (24), 13993–14000. <http://dx.doi.org/10.1021/es4039648>.
- Lu, Z., Streets, D.G., Zhang, Q., Wang, S., Carmichael, G.R., Cheng, Y.F., Wei, C., Chin, M., Diehl, T., Tan, Q., 2010. Sulfur dioxide emissions in China and sulfur trends in East Asia since 2000. *Atmos. Chem. Phys.* 10 (13), 6311–6331. <http://dx.doi.org/10.5194/acp-10-6311-2010>.
- Luo, Y., Zheng, X., Zhao, T., Chen, J., 2014. A climatology of aerosol optical depth over China from recent 10 years of MODIS remote sensing data. *Int. J. Climatol.* 34, 863–870. <http://dx.doi.org/10.1002/joc.3728>.
- McLinden, C.A., Fioletov, V., Boersma, K.F., Kharol, S.K., Krotkov, N., Lamsal, L., Makar, P.A., Martin, R.V., Veefkind, J.P., Yang, K., 2014. Improved satellite retrievals of NO₂ and SO₂ over the Canadian oil sands and comparisons with surface measurements. *Atmos. Chem. Phys.* 14 (7), 3637–3656. <http://dx.doi.org/10.5194/acp-14-3637-2014>.
- McLinden, C.A., Fioletov, V., Boersma, K.F., Krotkov, N., Sioris, C.E., Veefkind, J.P., Yang, K., 2012. Air quality over the Canadian oil sands: a first assessment using satellite observations. *Geophys. Res. Lett.* 39 (4) <http://dx.doi.org/10.1029/2011GL050273>.
- McLinden, Chris, A., Vitali Fioletov, Shephard, Mark W., Krotkov, Nick, Li, Can, Martin, Randall V., Moran, Michael D., Joiner, Joanna, 2016. Space-based detection of missing sulfur dioxide sources of global air pollution. *Nat. Geosci.* <http://dx.doi.org/10.1038/ngeo2724>.
- Munro, R., Lang, R., Klaes, D., et al., 2016. The GOME-2 instrument on the Metop series of satellites: instrument design, calibration, and level 1 data processing – an overview. *Atmos. Meas. Tech.* 9, 1279–1301. <http://dx.doi.org/10.5194/amt-9-1279-2016>.
- Platt, U., Stutz, J., 2008. *Differential Optical Absorption Spectroscopy (DOAS): Principle and Applications*. Springer, Berlin.
- Rix, M., Valks, P., Hao, N., Loyola, D., Schlager, H., Huntrieser, H., Flemming, J., Koehler, U., Schumann, U., Inness, A., 2012. Volcanic SO₂, BrO and plume height estimations using GOME-2 satellite measurements during the eruption of Eyjafjallajökull in May 2010. *J. Geophys. Res.* 117, D00U19. <http://dx.doi.org/10.1029/2011JD016718>.
- SCIAMACHY/Envisat Algorithm Description (ATBD) (2015): Lichtenberg, G., Bovenmann, H., Van Roozendael, M., Doicu, A., Eichmann, K.-U., Hess, M., Hrechanny, S., Kokhanovsky, A., Lerot, C., Noel, S., Richter, A., Rozanov, A., Schreier, F. and Tilstra, L.G., SCIAMACHY Offline Level 1b-2 Processor ATBD, ENV-ATB-QWG-SCIA-0085, 2010, issue 1A, http://atmos.caf.dlr.de/sciamachy/documents/level_1b_2/sciaol1b2_atbd_master.pdf, (last accessed: 16.06.15.).
- SCIAMACHY/Envisat SGP 5.02 Level-2 products Readme File issue 1.2, (2011), https://earth.esa.int/documents/700255/708683/SCIAMACHY+L2+Quality+Readme+file/db993046-d18c-40ed-b6e6-5c4b474ab7a5_ENVI-GSOP-EOGD-QD-13-0118, (last accessed: 16.06.16.).
- Taylor, M., Koukoulis, M.E., Theys, N., et al., 2016b. A Robust Seasonality Detector for Time Series Affected by Periodic Drivers and Sporadic Events; Application to SO₂ Observations over China, XIII EMTN National-international Conference of Meteorology-Climatology and Atmospheric Physics, Springer Atmospheric Sciences, Perspectives on Atmospheric Sciences. ISBN : 978-3-319-35094-3, September 19–21, Thessaloniki, Greece.
- Taylor, M., Koukoulis, M.E., Theys, N., et al., 2016a. A Robust Seasonality Detector for Time Series Affected by Periodic Drivers and Sporadic Events; Application to Satellite SO₂ Estimates. in preparation for submission to *Nonlinear Processes in Geophysics*.
- Theys, N., Van Gent, J., van Roozendael, M., et al., 2013. Interim Verification Report of GOME-2 GDP 4.7 SO₂ Column Data for MetOp-B Operational Readiness Review, Technical Note/Validation Report SAF/O3M/IASB/VR/SO2/TN-iasb-gome2b-O3MSAF-SO2-2013), O3M SAF. available at: http://o3msaf.fmi.fi/docs/vr/Validation_Report_OTO_SO2_Jun_2013.pdf (last access: 21.04.16.).
- Theys, N., De Smedt, I., van Gent, J., Danckaert, T., Wang, T., Hendrick, F., Stavrou, T., Bauduin Clarisse, L., Li, C., Krotkov, N., Yu, H., Brenot, H., Van Roozendael, M., 2015. Sulfur dioxide vertical column DOAS retrievals from the Ozone Monitoring Instrument: global observations and comparison to ground-based and satellite data. *J. Geophys. Res. Atmos.* 120 (6), 2470–2491. <http://dx.doi.org/10.1002/2014JD022657>.
- van der A, R.J., Mijling, B., Ding, J., Koukoulis, M.E., Liu, F., Li, Q., Mao, H., Theys, N., 2016. Cleaning up the air: effectiveness of air quality policy for SO₂ and NO_x emissions in China. *Atmos. Chem. Phys. Discuss.* <http://dx.doi.org/10.5194/acp-2016-445> in review.
- Vandaele, A.C., Simon, P.C., Guilmet, M., Carleer, M., Colin, R., 1994. SO₂ absorption cross section measurement in the UV using a Fourier transform spectrometer. *J. Geophys. Res.* 99, 25599–25605.
- Zerefos, C., Ganev, K., Kourtidis, K., Tzortziou, M., Vasaras, A., Syrakov, E., 2000. On the origin of SO₂ above Northern Greece. *Geophys. Res. Lett.* 27 (3) <http://dx.doi.org/10.1029/1999GL010799>.
- Zhang, Q., Streets, D.G., He, K., 2009. Satellite observations of recent power plant construction in Inner Mongolia, China. *Geophys. Res. Lett.* 36 (15) <http://dx.doi.org/10.1029/2009GL038984>.
- Zhu, Z.M., Han, G., Gong, W., Cui, Z.Z., Zhang, M., 2015. Study on long-term trend of atmospheric contaminants in Wuhan. *J. HuaZhong Normal Univ. Nat. Sci. Ed.* 49 (2), 280–286.
- Zoogman, P., et al., 2016. Tropospheric emissions: monitoring of pollution (TEMPO). *J. Quant. Spectrosc. Radiat. Transf.* <http://dx.doi.org/10.1016/j.jqsrt.2016.05.008>.